

Structural and mechanistic insight into Holliday-junction dissolution by Topoisomerase III α and RMI1

Nicolas Bocquet¹, Anna H Bizard², Wassim Abdulrahman¹, Nicolai B Larsen², Mahamadou Faty¹, Simone Cavadini¹, Richard D Bunker¹, Stephen C Kowalczykowski³, Petr Cejka^{3,4}, Ian D Hickson² & Nicolas H Thomä¹

Repair of DNA double-strand breaks via homologous recombination can produce double Holliday junctions (dHJs) that require enzymatic separation. Topoisomerase III α (TopIII α) together with RMI1 disentangles the final hemicatenane intermediate obtained once dHJs have converged. How binding of RMI1 to TopIII α influences it to behave as a hemicatenane dissolvase, rather than as an enzyme that relaxes DNA topology, is unknown. Here, we present the crystal structure of human TopIII α complexed to the first oligonucleotide-binding domain (OB fold) of RMI1. TopIII α assumes a toroidal type 1A topoisomerase fold. RMI1 attaches to the edge of the gate in TopIII α through which DNA passes. RMI1 projects a 23-residue loop into the TopIII α gate, thereby influencing the dynamics of its opening and closing. Our results provide a mechanistic rationale for how RMI1 stabilizes TopIII α -gate opening to enable dissolution and illustrate how binding partners modulate topoisomerase function.

Homologous recombination (HR) is a central pathway for the repair of DNA double-strand breaks and single-stranded gaps and is required for the maintenance and restarting of stalled replication forks^{1,2}. HR uses a homologous DNA sequence as a template for the repair of the damaged DNA strand. In canonical HR, after DNA synthesis and ligation, a dHJ intermediate is produced, which typically interconnects two sister chromatids^{3,4}. These dHJ intermediates are processed, in either a crossover or a noncrossover fashion^{5–7} to produce recombinant products. Several nucleases are able to cleave the symmetrical Holliday junction to yield an equal number of crossover or noncrossover products. Mitotic crossovers, however, carry the risk of loss of heterozygosity (LOH), a known driver of oncogenic transformation^{8,9}. In mitotic cells, LOH appears to be rare, contributing to only 2.5% of HR-mediated double-strand-breakage repair events¹⁰. Alternative pathways must therefore exist to bias HR events toward a noncrossover outcome.

The DNA molecules within the dHJ intermediate are topologically linked. The disjunction of the entangled chromosomes can be accomplished through the duplex-unwinding activity of a specific helicase coupled to DNA-strand unlinking by a type 1A topoisomerase. The interplay between RecQ helicases and topoisomerases, which is conserved in all kingdoms of life, exclusively generates noncrossover products¹¹ via a process termed dHJ dissolution. In humans, TopIII α acts with BLM¹¹, a RecQ helicase that is mutated in the cancer-predisposition disorder Bloom's syndrome. The yeast counterparts of these proteins are Top3 topoisomerase and Sgs1 helicase^{12–14}. Although Sgs1 (BLM) and Top3 (TopIII α) are required to process various topologically linked substrates^{15,16}, they act in concert with an additional essential component: Rmi1 in yeast^{17,18} and the RMI1–RMI2

complex in humans^{19–21}. Together, the RecQ helicase, Top3 (TopIII α) and Rmi1 (RMI1) proteins form the minimal dHJ dissolvosome. Loss or mutation of any component of this complex results in genomic instability^{18,22,23}.

The dHJ dissolution involves first a branch-migration step that requires a helicase (BLM or Sgs1)²⁴ to make the junctions migrate toward each other and a topoisomerase (TopIII α or Top3) to relieve positive supercoiling between the migrating junctions^{25–27}. This process collapses the two HJs into a hemicatenane, and it is followed by a decatenation step that unhooks the hemicatenane intermediate into two separate DNA duplexes^{25,26}.

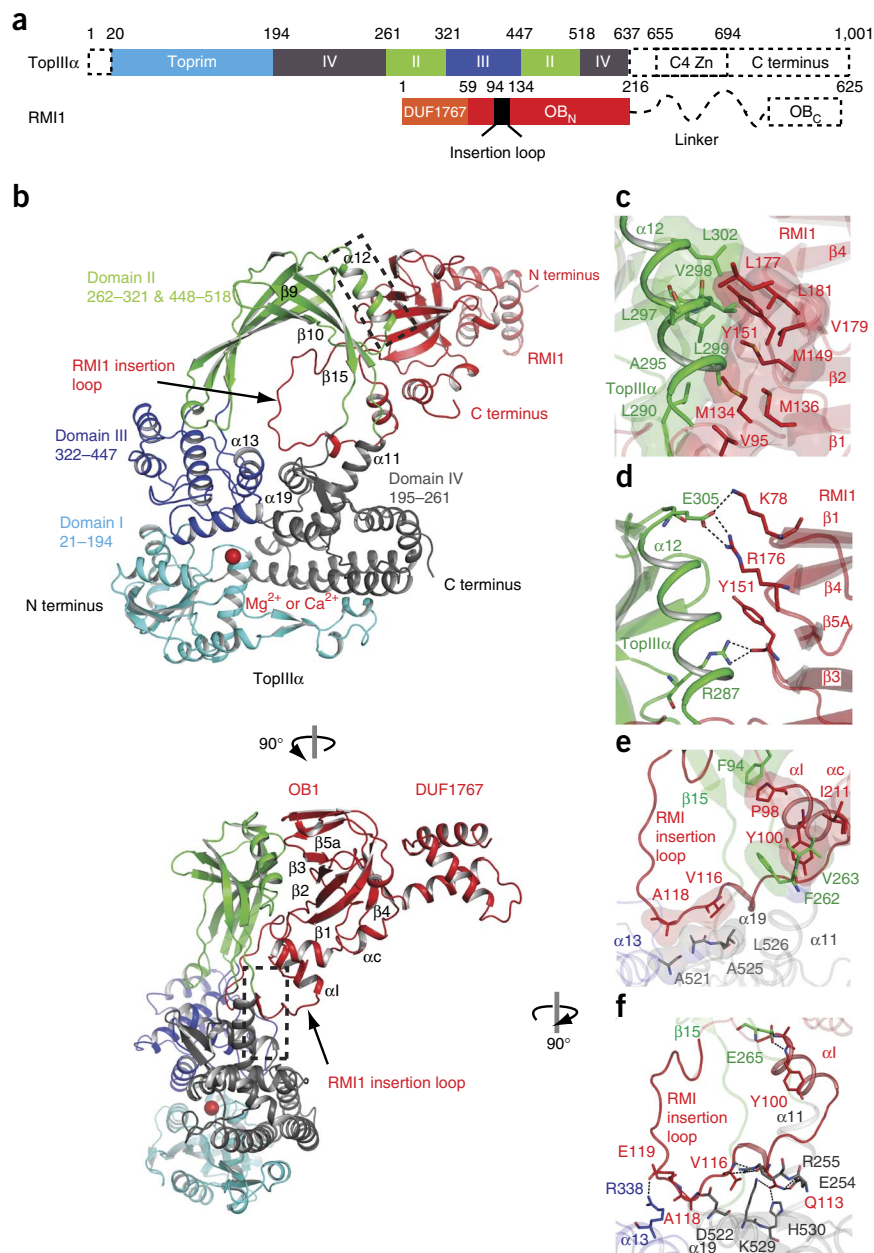
TopIII α is a member of the type 1A family of topoisomerases, which form a toroidal structure and introduce a transient single-stranded nick in one DNA strand (cut strand or C strand), thus allowing a second single-stranded DNA (ssDNA) strand to be transferred reversibly through the nick (transfer strand or T strand). When T and C strands belong to separate duplexes, the outcome is decatenation or catenation (or, alternatively, hemicatenation if only one strand is moved) and in the case of an HJ substrate, dHJ dissolution or dHJ formation. Should the T and C strands belong to the same, plectonemically linked duplex, relaxation then occurs. The in-and-out movement of a DNA single strand (T strand) is made possible by a gate of intertwined β -sheets allowing reversible opening and closing of the torus²⁸. In this context, the C strand is cut in a reversible transesterification process giving rise to a 5'-phosphotyrosine ssDNA intermediate, with the T strand being passed through the nick²⁹. Top3 and TopIII α , in isolation, are moderately effective in relaxing negatively supercoiled plasmids, but they do possess modest ssDNA-decatenase activity³⁰. In yeast, as in humans²¹, efficient decatenation requires

¹Friedrich Miescher Institute for Biomedical Research, Basel, Switzerland. ²Center for Healthy Aging, Department of Cellular and Molecular Medicine, University of Copenhagen, Copenhagen, Denmark. ³Department of Microbiology and Molecular Genetics, University of California, Davis, Davis, California, USA. ⁴Present address: Institute of Molecular Cancer Research, University of Zürich, Zürich, Switzerland. Correspondence should be addressed to N.H.T. (nicolas.thoma@fmi.ch).

Received 15 March 2013; accepted 17 January 2014; published online 9 February 2014; doi:10.1038/nsmb.2775

Figure 1 Overall architecture and TopIII α -RMI1 binding interface. (a) Domain organization of the human TopIII α -RMI1 complex.

(b) Overall architecture of the crystallized complex showing domains I, toprim domain (cyan); II, gate domain with the two topo-fold domains (green); III, catalytic 5Y cap (dark blue); and IV, noncatalytic CAP domain (gray). RMI1 is shown in red. The catalytic metal is represented by a red sphere. (c) Hydrophobic zipper between RMI1 residues originating from OB_N and residues originating from the α 12 and β 10- α 12 gate of TopIII α . (d) As in c but depicting the corresponding hydrogen-bonding network. (e) Interaction between the RMI1-loop segment and the hydrophobic patch of the TopIII α gate (helix α 19) (near proposed pivot point shown in Fig. 5). RMI1 P98 is engaged in hydrophobic stacking with TopIII α residue F94; neighboring RMI1 Y100 stacks with TopIII α F262. (f) Similar to e, highlighting the corresponding hydrogen-bonding and salt-bridge network. RMI1 Q113 is at the center of a hydrogen-bonding network binding TopIII α E254, H530 and K529 while ionic interaction between RMI1 E119 and TopIII α R338 locks the RMI1 insertion loop in position.



the presence of Rmi1, which also serves to inhibit the relaxation activity²⁵. Biochemical analysis of this regulatory behavior led to the discovery that Rmi1 increases the steady-state level of the so-called open complex of Top3 and suggested a model in which Rmi1 stabilizes the open conformation of the topoisomerase gate²⁵. The structural basis by which RMI1 (Rmi1) modulates gating of strand passage by TopIII α (Top3) and bestows efficient decatenation functionality that allows dHJ dissolution has remained elusive.

We set out to define how RMI1 (Rmi1) modulates TopIII α (Top3) function by using structural and biochemical approaches. We show that RMI1 modulates the dynamics of the topoisomerase action through a loop lining the topoisomerase gate.

RESULTS

Construct design of the TopIII α -RMI1 complex

Human TopIII α and yeast Top3 carry distinct sequence signatures that distinguish them from their prokaryotic Top3 counterparts (Supplementary Figs. 1 and 2). In the absence of structural information, it is unclear to what extent the eukaryotic TopIII α (Top3) decatenases have diverged from their prokaryotic counterparts and how RMI1 modulates topoisomerase function by promoting decatenase activity. In an effort to address these questions, we determined the structure of the TopIII α -RMI1 complex. We obtained crystals of the human TopIII α -RMI1 complex after 4–5 d for human TopIII α (residues 1–753 after deletion of residues 754–1001) in complex with human RMI1 (DUF1767 + N-terminal OB (OB_N), residues 1–219) (Fig. 1) in the presence of Mg²⁺ (200 mM MgCl₂) or Ca²⁺ (200 mM calcium citrate), which belonged to space group *P*4₁2₁2 with one heterodimer in the crystallographic asymmetric unit (Supplementary Fig. 3).

The TopIII α _{1–753} and RMI1_{1–219} constructs used in crystallization, when tested together with BLM, remained active in dHJ dissolution (Supplementary Fig. 4a), thus suggesting that these boundaries are sufficient for dissolution. We solved the structure of Mg²⁺-bound TopIII α in complex with RMI1 (TopIII α -Mg²⁺-RMI1) by molecular replacement and refined it to a maximal resolution of 2.85 Å. The model has good agreement with the diffraction data (Table 1) and excellent validation statistics. We also determined the structure of a crystal grown in the presence of Ca²⁺, TopIII α -Ca²⁺-RMI1, at 3.25-Å resolution, and it has similar validation statistics. The domain boundaries for the human TopIII α -RMI1 (OB_N) complex used for crystallization are equivalent to those of full-length *Saccharomyces cerevisiae* Top3-Rmi1. Human RMI1 encompasses a DUF1767 three- α -helix bundle followed by an N-terminal (OB_N) and a C-terminal (OB_C) oligonucleotide-binding domain^{17,20} (Fig. 1a,b). OB_C, which is absent in yeast, is responsible for RMI2 binding in the human complex^{31,32}. Deletion of human RMI1 OB_C has no adverse effect

Table 1 Data collection and refinement statistics

	TOPIII α -Mg ²⁺ -RMI1	TOPIII α -Ca ²⁺ -RMI1
Data collection		
Space group	<i>P</i> 4 ₁ 2 ₁ 2	<i>P</i> 4 ₁ 2 ₁ 2
Cell dimensions		
<i>a</i> , <i>b</i> , <i>c</i> (Å)	94.00, 94.00, 331.72	93.38, 93.38, 331.62
Resolution (Å) ^a	62.78–2.85 (2.97–2.85)	65.05–3.25 (3.45–3.25)
<i>R</i> _{merge} (%)	14.9 (163)	16.1 (78.1)
<i>R</i> _{meas} (%)	16.0 (175)	19.7 (96.2)
<i>R</i> _{pim} (%)	4.2 (44.8)	8.4 (41.8)
CC _{1/2} outer shell; number of pairs ^b	0.814; <i>n</i> = 4,527	0.727; <i>n</i> = 4,328
<i>I</i> / σ <i>I</i>	16.7 (2.2)	8.2 (2.0)
Completeness (%)	100 (100)	99.8 (99.9)
Redundancy	14.1 (14.7)	5.3(5.3)
Refinement		
Resolution (Å)	2.85 Å	3.25 Å
No. reflections	41,328 (4,527)	27,765 (4,404)
<i>R</i> _{work} / <i>R</i> _{free}	19.7 / 23.1 (24.0 / 27.6)	19.7 / 22.5 (25.1 / 27.8)
No. atoms		
Protein	6,557	6,632
Ion	1	1
Water	45	5
<i>B</i> factors (Å ²)		
Protein	80.3	83.5
Ion	62.3	81.8
Water	59.0	78.9
r.m.s. deviations		
Bond lengths (Å)	0.009	0.010
Bond angles (°)	1.04	1.06

^aValues in parentheses are for highest-resolution shell. ^bRandom half-set (Pearson) correlation coefficient as defined in ref. 53.

on dHJ dissolution *in vitro*; thus, TopIII α -BLM-RMI1 (DUF1767 + OB_N) is the minimal functional dissolvosome complex³².

Overview of the TopIII α -RMI1 complex

The overall shape of the TopIII α -RMI1 complex resembles a brass doorknocker (Fig. 1b), with TopIII α forming the ring and RMI1 acting as its base. In the crystal, RMI1 makes distinct interactions with two TopIII α molecules. We additionally confirmed the biological TopIII α -RMI1 unit by single-particle EM (Fig. 1b and Supplementary Fig. 3).

Human TopIII α displays the canonical toroidal topoisomerase shape found in all type 1A family members solved to date (Fig. 1b)^{33–35}. Members of this family contain five characteristic domains: domain I, or topim (topoisomerase-primase), an acidic cluster (residues D148, D150 and E152) that binds the metal-ion cofactor required for C-strand cleavage^{28,36}; domain II, which creates the ~26-Å-diameter

Figure 2 Catalytic site of human TopIII α . (a) TopIII α catalytic-site residues and the Mg²⁺-binding site. Mg²⁺ is shown as a red sphere, with corresponding water molecules depicted as gray spheres. Simulated annealing composite $2mF_o - DF_c$ omit electron density map contoured at 1.5 σ (gray). The omit difference map shows peaks (green) for water molecules before their inclusion into the model. E41 serves as the sole residue directly contacting Mg²⁺, and D150 bridges a water molecule from the hydration shell. (b) Structural alignment of different catalytic centers taken from the available type 1A topoisomerase structures: *E. coli* Top3 in the apo state (PDB 1D6M³⁵) in cyan, *E. coli* Top1A in the apo state (PDB 1ECL³³) in magenta, Top1A from *T. maritima* (PDB 2GA1³⁴) in gray and *Homo sapiens* TopIII α (PDB 4CGY) in green. Mg²⁺ is shown as a red sphere.

topoisomerase gate formed with two antiparallel topo-fold domains³⁷; domain III, which forms winged-helix folds^{38,39} and carries the catalytic tyrosine (Y362) needed for ssDNA cleavage and formation of the 5'-phosphotyrosine ssDNA intermediate²⁹; domain IV, which shares the same winged-helix fold with domain III; and domain V in the C-terminal region (residues 655–1001), which includes a predicted zinc-finger motif (residues 655–694). Although domains I to IV are well defined in our structure, density for the N-terminal part of domain V (residues 638–753) could not be unambiguously assigned and have been omitted from the model. We observed no detectable Zn²⁺ anomalous signal.

RMI1 binds the toroidal TopIII α structure via its OB_N β -barrel domain at a site diametrically opposite to the topim ssDNA-binding site, with the RMI1 N terminus projecting away from the topoisomerase. RMI1 attaches to the top of the topoisomerase (domain II) gate, using an interface frequently used by other OB fold-containing proteins when binding protein ligands, sugars or oligonucleotides⁴⁰ (Fig. 1c,d). RMI1 projects a large insertion loop, located between β 1 and β 2, into the central gate of the topoisomerase (Fig. 1b,e,f and Supplementary Fig. 4b,c). In the structure of isolated RMI1, this loop has been shown to be partially disordered and to be involved in TopIII α binding³². The arrangement of the RMI1-TopIII α complex places the RMI1 insertion loop, which is not stabilized by crystal contacts, at the center of the topoisomerase gate (Supplementary Fig. 4c).

Mechanism of ssDNA cleavage

TopIII α showed a strong positive $mF_o - DF_c$ difference electron density at the topim acidic-residue cluster (Fig. 2a) and an anomalous signal peak at the same location corresponding to one calcium ion in TopIII α -Ca²⁺-RMI1. We note that Mg²⁺ and Ca²⁺ permitted crystallization and support catalysis⁴¹, but neither Zn²⁺ or Cs⁺ allowed crystallization. Given the Mg²⁺ dependence of DNA relaxation, the coordination chemistry observed and the proximity of the density to the acidic cluster, we assigned the $mF_o - DF_c$ electron density as Mg²⁺ in TopIII α -Mg²⁺-RMI1 (Ca²⁺ in TopIII α -Ca²⁺-RMI1). The metal ion is coordinated by five water molecules and one carboxylic oxygen of E41 in an octahedral configuration. The hydroxyl group of Y362 and carboxylic oxygen atoms of E352 point toward the water molecules and are well located to potentially form hydrogen bonds. D150 provides additional hydrogen bonds to bridge water molecules within the hydration shell (Fig. 2a). E352, conserved in eukaryotic orthologs (Fig. 2b and Supplementary Figs. 1 and 2a) is not part of the previously identified acidic cluster in *Escherichia coli* topoisomerases, in which it is substituted by a glutamine. Key residues serving comparable roles in eukaryotic and prokaryotic type 1A enzymes include R364, which is involved in pentavalent phosphate transition-state stabilization, and H414, which is implicated in anchoring cut ssDNA to the (-1) position^{42,43} (Fig. 2b).

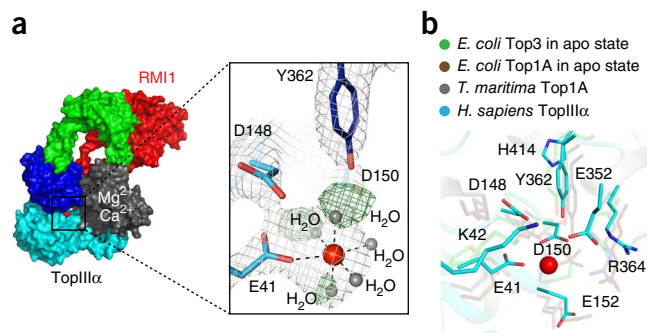
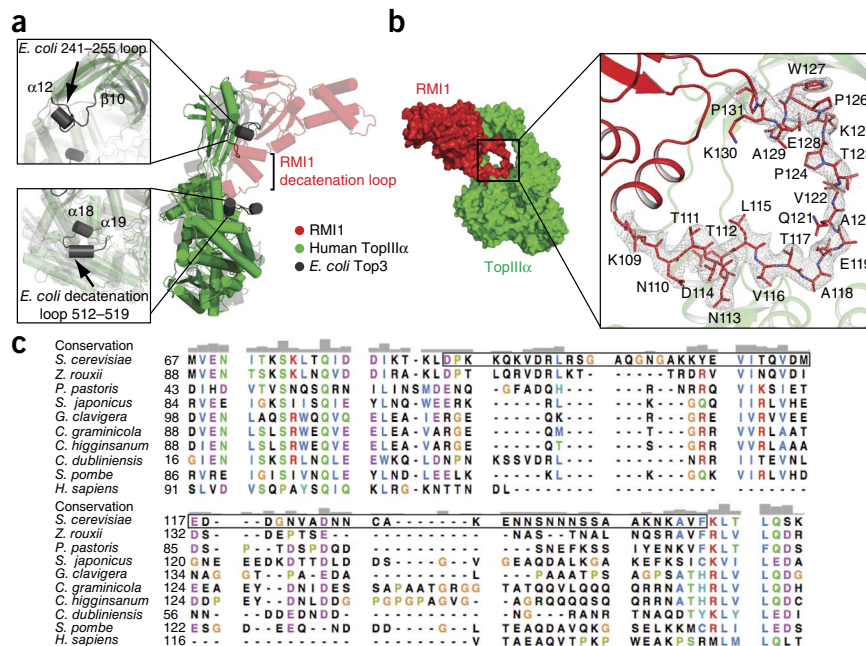


Figure 3 The RMI1 decatenation loop. (a) Comparison between *E. coli* Top3 (gray) and human TopIII α (green). RMI1 (red) inserts motifs at sites where *E. coli* Top3 diverges from human TopIII α . The two unique *E. coli* Top3 loop segments shown are the loop between residues 241 and 255 and the decatenation loop (502–519). (b) The final TopIII α -Ca²⁺-RMI1 model overlaid with an unbiased $2mF_o - DF_c$ electron density envelope calculated before modeling of the RMI1 decatenation loop, contoured at 1σ . (c) Sequence alignments between different yeast strains and human RMI1. Regions in the black-outlined box within the *S. cerevisiae* sequence have been randomized in the rRmi1 construct (Online Methods). Sequences for *S. cerevisiae*, *Zygosaccharomyces rouxii*, *Pichia pastoris*, *Obchizosaccharomyces japonicus*, *Grossmannia clavigera*, *Colletotrichum graminicola*, *Colletotrichum higginsanum*, *Candida dubliniensis*, *Schizosaccharomyces pombe* and *H. sapiens* are shown.



Whereas previous structures of prokaryotic type 1A topoisomerases did not show signs of bound catalytic metal ions, the TopIII α -RMI1 structure now provides insight into type 1A metal-mediated ssDNA cleavage. We find one Mg²⁺ or Ca²⁺ ion in our structures, with no indication of further binding sites. Instead, a lysine residue (K42), conserved within the topoisomerase type 1A family (Fig. 2b) is situated at the site equivalent to that of the second metal ion in TopII⁴⁴. K42 is ideally positioned to stabilize the negatively charged pentavalent-phosphate transition state arising during transesterification, thus serving a functionally equivalent role to the second metal ion. Our findings, therefore, favor a one-metal catalytic mechanism within the type 1A topoisomerase family, as proposed previously⁴⁴.

TopIII α resembles a prokaryotic type1A relaxase

TopIII α domains I, III and IV share close structural similarity with the Top1A relaxases from *E. coli* and *Thermatoga maritima* (r.m.s. deviation of 1.6 Å over 480 C α positions; Supplementary Figs. 1 and 2a), whereas the similarity with the *E. coli* Top3 decatenase is less pronounced (r.m.s. deviation of 2.7 Å) (Fig. 3a). The most apparent differences between TopIII α and the prokaryotic Top3 decatenases (encoded by *topB*), however, are the absence of two loops equivalent to *E. coli* residues 241–255 (*E. coli* Top3 numbering; domain II) and 502–519 (domain IV), both lining the central cavity of the topoisomerase (Fig. 3a). The latter has been implicated in decatenation in the prokaryotic Top3 family (and is henceforth referred to as the decatenation loop)^{35,45}. Thus TopIII α , at the structural level, has close resemblance to a relaxase and does not display obvious structural features characteristic of prokaryotic type 1A decatenases.

The RMI1-TopIII α interface

RMI1 OB_N attaches to the TopIII α gate and acts as the major binding interface, occupying a total surface area of 1,565 Å². This interface is mainly hydrophobic in nature, with alkyl chains from RMI1 L177, L181 (β 4– β 5A loop), V179 (β 5A strand), the aromatic ring of Y151 (β 3– β 4 loop) and methionines M134, M136 and M149 (α 1, β 2 strand and β 3 strands, respectively) forming a hydrophobic zipper with TopIII α L302, L297, V298, L299 and A295 on α 12, and L290 on the β 10– α 12 loop (Fig. 1c). These residues form a hydrophobic

groove that accommodates TopIII α helix α 12. RMI1 OB_N-domain residues K78 and R176 (β 4– β 5A) form a bifurcated salt bridge with TopIII α E305 and further stabilize binding (Fig. 1d).

The RMI1 insertion loop inserts into the TopIII α gate

The RMI1 loop, residues 94–134, which is inserted between RMI1 strands β 1 and β 2, lines the gate of the topoisomerase (Figs. 1b and 3b). In the structures of the two TopIII α -RMI1 complexes, the loop differs slightly: although being less ordered in TopIII α -Mg²⁺-RMI1 (Supplementary Fig. 4c–e) with an apparent discontinuity of the electron density around residues 120 and 131, the RMI1 insertion loop can be fully traced in the electron density maps obtained with the TopIII α -Ca²⁺-RMI1 data (Fig. 3b). Hence, the TopIII α -Ca²⁺-RMI1 complex will subsequently be used as the basis for discussion. The RMI1 insertion loop emanates from β 1 (D94) and protrudes into the TopIII α gate, creating two layers of aligned and parallel rings (Fig. 1b). Residues from the insertion loop of RMI1 form tight intercalated hydrophobic stacking interactions with the TopIII α gate. Most prominently, RMI1 P98 and Y100 stack against TopIII α F94, F262 and V263 (Fig. 1e,f). This region in TopIII α , by structural analogy to the *E. coli* topoisomerase 1, is expected to serve as a pivot point for gate opening⁴⁶.

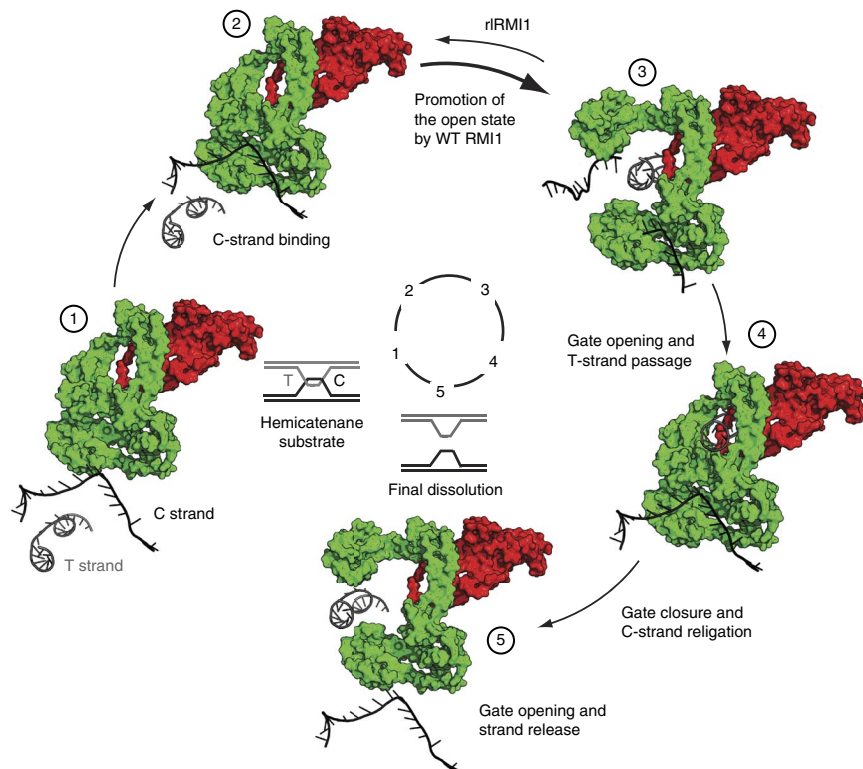
In the conformational state trapped in the crystal, the RMI1 insertion loop restricts the size of the central opening in the TopIII α gate from 25 Å to 13 Å. Because the ssDNA has to be moved into the central cavity through an opening between domains I and III, the topoisomerase gate is effectively closed when occupied by the RMI1 insertion loop (Fig. 1b).

When examining the structure of the TopIII α -RMI1 complex, we note that in regions where the TopIII α structure diverges from that of the *E. coli* Top3 decatenase, RMI1 donates structural motifs *in trans* (Fig. 3a,b). We therefore focused on the RMI1 insertion loop, examining whether decatenation ability could principally be provided by RMI1 structural motifs.

Decatenation and dHJ dissolution *in vitro*

To functionally dissect the contribution of the RMI1 insertion loop within the TopIII α -RMI1 complex, we switched to yeast as a model

Figure 5 Model for the final steps of dHJ dissolution catalyzed by TopIII α -RMI1. The model depicts the TopIII α -RMI1 catalytic cycle with the decatenation of a hemicatenane, the final product of the dHJ dissolution process, taken as an example. TopIII α (in green) loads onto the DNA substrate (1) and introduces a nick in the C strand (2), thus generating a gap through which the T strand can pass after opening of the gate (3). RMI1 (red) stabilizes step 3, allowing sufficient time to move a DNA strand (T strand) originating from a second, separate DNA duplex into the gate. After gate closure (4), the substrate is released (5), and the decatenation process is completed.



dependent on Sgs1, *E. coli* single-strand-binding protein (SSB), which can replace yeast RPA protein (the cognate ssDNA-binding protein), and Top3 (Supplementary Fig. 5c). These data suggest that the Rmi1 loop, with its ability to stabilize the open state of Top3, is also required for decatenation and dHJ dissolution *in vitro*. We subsequently refer to the Rmi1 insertion loop (residues 94–134) as the Rmi1 decatenation loop.

In an effort to further define the region within the Rmi1 decatenation loop required for dHJ dissolution, we reverted to the human TopIII α -RMI1 system and engineered two deletion constructs: L₁RMI1, with a Ser-Gly-Ser-Gly insertion between residues P98 and P131, and L₂RMI1, with an Ala-Gly-Gly-Ser-Gly-Ser-Gly linker inserted between L115 and P131 (Fig. 4e,f). L₁RMI1 links the loop at its most narrow point, retaining only the interaction between the RMI1 OB_N and the TopIII α gate and hence removing the decatenation loop. In contrast, L₂RMI1 retains the TopIII α interaction with RMI1 OB_N and the N-terminal half of the RMI1 loop (Fig. 1e,f), the latter also being the most conserved portion of the decatenation loop between yeast and human proteins (Fig. 4f). Whereas L₂RMI1 had near wild-type ability to stimulate dHJ dissolution, L₁RMI1 showed an impairment of approximately 50% relative to wild-type stimulation, and the activity could not be rescued by addition of higher concentrations of RMI1 (quantified in Fig. 4e,g). We conclude, therefore, that human RMI1-loop residues 99–116 contribute to the decatenation process and that the RMI1 decatenation loop is required for dissolution mediated by TopIII α -RMI1 in the human and yeast complexes.

DISCUSSION

We have determined the structure of the human TopIII α -RMI1 (OB_N) complex and have found strong resemblance between TopIII α and prokaryotic type 1A topoisomerases. Dissolution of a synthetic Holliday junction is dependent on the RMI1 decatenation-loop segment, which is donated *in trans* into the central gate of the topoisomerase. To illustrate what we propose happens in the TopIII α -RMI1 reaction cycle, we built a TopIII α model, representing different stages of decatenation, based on known structures and simulations available for *E. coli* Top1A^{46,47}. This model depicts domain III and the gate in a presumed open conformation (Fig. 5) and suggests that the gate may create an opening of up to 30 Å in width, analogously to what has been suggested for *E. coli* TopIA⁴⁶. For the topoisomerase cycle to be completed, the T strand has to be moved through the C-strand nick, and subsequent C-strand religation and DNA release must

occur (Fig. 5). A certain degree of plasticity within the decatenation loop is thus required to accommodate the ssDNA upon gate closure, because the cavity between the decatenation loop and the topoisomerase gate measures only around 11 Å at its widest point (with the diameter of ssDNA being approximately 7 Å). This is in line with the plasticity of the decatenation loop observed when comparing the Mg²⁺- and Ca²⁺-bound crystal forms (Fig. 3b and Supplementary Fig. 4d,e). In the Mg²⁺-bound structure, the loop segment is disordered around this presumed ssDNA T-strand-binding site (residues 116–131). This site is also the locus where the additional 39 residues within the *S. cerevisiae* Rmi1 loop are inserted, thus further supporting the notion that conformation variability exists at this site (Fig. 3c). Because truncation or substitution of the tip of the loop in the human L₂Rmi1 mutant gave rise to only very minor dHJ dissolution defects *in vitro* (Fig. 4e), we conclude that this part of the loop, which is likely to be in direct contact with DNA, exerts neither crucial attractive (through charged or hydrophobic residues) nor repulsive (through steric crowding) interactions with DNA. Despite the necessary plasticity of the loop in this region, the presence of the RMI1 OB_N domain and its attachment points within the gate (Fig. 2b) impart steric constraints that are expected to disfavor accommodation of double-stranded DNA within the TopIII α gate. This is in agreement with the low efficiency (approximately ten-fold less efficient than for ssDNA) by which double-stranded DNA is accommodated by the Top3-Rmi1 complex in decatenation experiments²⁵ and contrasts with the behavior seen with prokaryotic Top3 enzymes⁴⁸.

The RMI decatenation loop modulates the gate dynamic

In the model of the open form (Fig. 5, step 3), we observed that the pivot region of the gate is in proximity to the beginning of the RMI1 decatenation loop involving residues around P98–K109 (Fig. 1e). Experimentally we find that human RMI1 residues 96–116 are required for effective decatenation (Fig. 4e,g). In addition, RMI1 residues

ranging from P96 to K109 are also reasonably conserved among orthologs (Fig. 3c). We therefore hypothesize that this contact region between the RMI1 loop and TopIII α contributes to the modulation of the TopIII α opening-closing equilibrium.

Toward a unified mechanism for decatenation

Analysis of the TopIII α -RMI1 system has the great advantage that decatenation is stimulated by RMI1 addition *in trans*, thus allowing direct probing of the effect of RMI1 on decatenation without manipulation of the topoisomerase itself. Prokaryotic type IA topoisomerases implicated in relaxation and those involved in decatenation (for example, *E. coli* Top3) share almost identical enzymatic cores with only minimal structural differences. The most striking difference is the presence or absence of the decatenation loop lining the gate, which is found exclusively in the prokaryotic decatenases³⁵. Deletion of this loop in *E. coli* Top3 results in almost complete loss of decatenation activity, albeit with relaxation activity also being impaired⁴⁵. The structural equivalent of this loop in the eukaryotic Top3 (TopIII α) decatenases is absent, a feature that has previously been used as an argument against loop-mediated decatenation. We now find that RMI1 inserts a loop segment, *in trans*, positioned in proximity to the two loci of the prokaryotic decatenation loop. Moreover, this loop in RMI1 is required for effective decatenation and dHJ resolution.

We propose a model based on our new data (Fig. 5), whereby after the binding and scission of the single-stranded C strand the topoisomerase gate opens. Although C-strand cleavage is not dependent on RMI1, the gate, once open, is stabilized through structural elements originating from the RMI1 loop (or possibly the functionally equivalent loops found in prokaryotic type IA enzymes). The structural and biochemical data support a model in which the gate in its stabilized open state will provide the topoisomerase with sufficient time to accommodate distant ssDNA T strands originating from different duplexes (for example, in dHJ dissolution). This permits the movement of these strands in and out of the gate, thereby driving decatenation (as an 'intermolecular process')²⁵. In contrast, in its relaxation mode, in which the T strand belongs to the same duplex as does the C strand (working in an intramolecular process), movement of DNA strands probably occurs over shorter distances and hence does not require extended gate-opening times.

TopIII α -RMI1 function in the dissolvasome

dHJ dissolution is dependent on the presence of a complete dissolvasome consisting, minimally, of TopIII α (Top3), RMI1 (Rmi1) and a RecQ helicase. In yeast, the Sgs1 RecQ helicase serves both a catalytic and noncatalytic scaffolding role. We now find that RMI1 does not fundamentally change the mode of topoisomerase action but instead modulates its dynamics and specificity, allowing the decatenation of a dHJ hemicatenane rather than relaxation. Further studies are required to understand how TopIII α -RMI1 functionally and structurally integrates within the RecQ-containing dissolvasome.

Conclusion

In the cell, the majority of proteins function in the context of macromolecular complexes. The structure of TopIII α -RMI1 illustrates how binding proteins modulate topoisomerase function within their large assemblies (also referred to as toposomes⁴⁹). Epitopes such as the RMI1 loop, which are unstructured in isolation, can nonetheless assume crucial catalytic and regulatory roles when put in the context of these macromolecular machines⁵⁰.

METHODS

Methods and any associated references are available in the [online version of the paper](#).

Accession codes. Coordinates of the models have been deposited in the Protein Data Bank under accession codes 4CGY for the TOPIII α -RMI1 structure bound to a Mg²⁺ ion and 4CHT for the TOPIII α -RMI1 structure bound to a Ca²⁺ ion.

Note: Any Supplementary Information and Source Data files are available in the online version of the paper.

ACKNOWLEDGMENTS

This work was supported by the Novartis Research Foundation (to N.H.T.), grants from the Krebsforschung Schweiz (KFS-2986-08-2012) (to N.H.T.), Marie Curie Fellowship (FP7-PEOPLE-2009-IEF 253555-TOPO) (to N.B.), European Molecular Biology Organization long-term Fellowship (EMBO ALTF 693-2009) (to N.B.) and European Research Council (to N.H.T. and I.D.H.), the Nordea Foundation (to I.D.H.), The Villum Kann Rasmussen Fund (to I.D.H.) and the US National Institutes of Health (GM-41347 and GM-62653) (to S.C.K.). We are grateful to H. Stahlberg and team for use of the EM facilities at the Center for Cellular Imaging and NanoAnalytics (c-CINA). We thank S. Gasser, U. Rass, K. Shimada, J. Keusch, E. Fischer, A. Scrima, D. Hess, K. Boehm, D. Klein, H. Gut and M. Renuat for help and fruitful discussion. We would also like to thank A. Costa and colleagues at the London Research Institute for sharing results prior to publication. Part of this work was performed at beamline PXII of the Swiss Light Source at the Paul Scherrer Institute, Villigen, Switzerland.

AUTHOR CONTRIBUTIONS

N.B. carried out molecular biology, protein expression and purification, crystallization, structure determination and model refinement. R.D.B. and N.H.T. carried out final stages of model refinement and map improvements. A.H.B. performed the relaxation, catenation and decatenation assays, with contributions by W.A. and N.B., and dissolution assays. W.A. did the M13-digest assay. N.B. performed the construct design, expression and purification of human RMI1-mutant proteins for dissolution assays. P.C. provided yeast Top3 and Sgs1 proteins as well as SSB protein. S.C. carried out single-particle EM and three-dimensional model reconstruction. M.F. and N.B.L. performed yeast-strain constructions and drop-assay tests. N.B. and N.H.T. designed the project with the help of P.C., S.C.K. and I.D.H.; N.B. and N.H.T. wrote the paper with the help of the other coauthors. N.H.T. supervised the project.

COMPETING FINANCIAL INTERESTS

The authors declare no competing financial interests.

Reprints and permissions information is available online at <http://www.nature.com/reprints/index.html>.

- Petermann, E. & Helleday, T. Pathways of mammalian replication fork restart. *Nat. Rev. Mol. Cell Biol.* **11**, 683–687 (2010).
- Moynahan, M.E. & Jasin, M. Mitotic homologous recombination maintains genomic stability and suppresses tumorigenesis. *Nat. Rev. Mol. Cell Biol.* **11**, 196–207 (2010).
- Holliday, R. A mechanism for gene conversion in fungi. *Genet. Res.* **89**, 285–307 (2007).
- Szostak, J.W., Orr-Weaver, T.L., Rothstein, R.J. & Stahl, F.W. The double-strand-break repair model for recombination. *Cell* **33**, 25–35 (1983).
- Heyer, W.D., Ehmsen, K.T. & Solinger, J.A. Holliday junctions in the eukaryotic nucleus: resolution in sight? *Trends Biochem. Sci.* **28**, 548–557 (2003).
- Matos, J., Blanco, M.G., Maslen, S., Skehel, J.M. & West, S.C. Regulatory control of the resolution of DNA recombination intermediates during meiosis and mitosis. *Cell* **147**, 158–172 (2011).
- Heyer, W.D. Recombination: Holliday junction resolution and crossover formation. *Curr. Biol.* **14**, R56–R58 (2004).
- Cavenee, W.K. *et al.* Expression of recessive alleles by chromosomal mechanisms in retinoblastoma. *Nature* **305**, 779–784 (1983).
- Thiagalingam, S. *et al.* Mechanisms underlying losses of heterozygosity in human colorectal cancers. *Proc. Natl. Acad. Sci. USA* **98**, 2698–2702 (2001).
- LaRocque, J.R. *et al.* Interhomolog recombination and loss of heterozygosity in wild-type and Bloom syndrome helicase (BLM)-deficient mammalian cells. *Proc. Natl. Acad. Sci. USA* **108**, 11971–11976 (2011).
- Wu, L. & Hickson, I.D. The Bloom's syndrome helicase suppresses crossing over during homologous recombination. *Nature* **426**, 870–874 (2003).

12. Gangloff, S., McDonald, J.P., Bendixen, C., Arthur, L. & Rothstein, R. The yeast type I topoisomerase Top3 interacts with Sgs1, a DNA helicase homolog: a potential eukaryotic reverse gyrase. *Mol. Cell. Biol.* **14**, 8391–8398 (1994).
13. Bennett, R.J., Noiro-Gros, M.F. & Wang, J.C. Interaction between yeast sgs1 helicase and DNA topoisomerase III. *J. Biol. Chem.* **275**, 26898–26905 (2000).
14. Fricke, W.M., Kaliraman, V. & Brill, S.J. Mapping the DNA topoisomerase III binding domain of the Sgs1 DNA helicase. *J. Biol. Chem.* **276**, 8848–8855 (2001).
15. Harmon, F.G., DiGate, R.J. & Kowalczykowski, S.C. RecQ helicase and topoisomerase III comprise a novel DNA strand passage function: a conserved mechanism for control of DNA recombination. *Mol. Cell* **3**, 611–620 (1999).
16. Cejka, P. & Kowalczykowski, S.C. The full-length *Saccharomyces cerevisiae* Sgs1 protein is a vigorous DNA helicase that preferentially unwinds Holliday junctions. *J. Biol. Chem.* **285**, 8290–8301 (2010).
17. Xu, D. *et al.* RMI, a new OB-fold complex essential for Bloom syndrome protein to maintain genome stability. *Genes Dev.* **22**, 2843–2855 (2008).
18. Mullen, J.R., Nallaseth, F.S., Lan, Y.Q., Slagle, C.E. & Brill, S.J. Yeast Rmi1/Nce4 controls genome stability as a subunit of the Sgs1-Top3 complex. *Mol. Cell. Biol.* **25**, 4476–4487 (2005).
19. Singh, T.R. *et al.* BLAP18/RMI2, a novel OB-fold-containing protein, is an essential component of the Bloom helicase-double Holliday junction dissolvosome. *Genes Dev.* **22**, 2856–2868 (2008).
20. Raynard, S., Bussen, W. & Sung, P. A double Holliday junction dissolvosome comprising BLM, topoisomerase III α , and BLAP75. *J. Biol. Chem.* **281**, 13861–13864 (2006).
21. Wu, L. *et al.* BLAP75/RMI1 promotes the BLM-dependent dissolution of homologous recombination intermediates. *Proc. Natl. Acad. Sci. USA* **103**, 4068–4073 (2006).
22. Lai, M.S., Seki, M., Ui, A. & Enomoto, T. Rmi1, a member of the Sgs1-Top3 complex in budding yeast, contributes to sister chromatid cohesion. *EMBO Rep.* **8**, 685–690 (2007).
23. Chang, M. *et al.* RMI1/NCE4, a suppressor of genome instability, encodes a member of the RecQ helicase/Topo III complex. *EMBO J.* **24**, 2024–2033 (2005).
24. Mankouri, H.W. & Hickson, I.D. The RecQ helicase-topoisomerase III-Rmi1 complex: a DNA structure-specific 'dissolvosome'? *Trends Biochem. Sci.* **32**, 538–546 (2007).
25. Cejka, P., Plank, J.L., Dombrowski, C.C. & Kowalczykowski, S.C. Decatenation of DNA by the *S. cerevisiae* Sgs1-Top3-Rmi1 and RPA complex: a mechanism for disentangling chromosomes. *Mol. Cell* **47**, 886–896 (2012).
26. Cejka, P., Plank, J.L., Bachrati, C.Z., Hickson, I.D. & Kowalczykowski, S.C. Rmi1 stimulates decatenation of double Holliday junctions during dissolution by Sgs1-Top3. *Nat. Struct. Mol. Biol.* **17**, 1377–1382 (2010).
27. Chen, C.F. & Brill, S.J. Binding and activation of DNA topoisomerase III by the Rmi1 subunit. *J. Biol. Chem.* **282**, 28971–28979 (2007).
28. Corbett, K.D. & Berger, J.M. Structure, molecular mechanisms, and evolutionary relationships in DNA topoisomerases. *Annu. Rev. Biophys. Biomol. Struct.* **33**, 95–118 (2004).
29. Tse, Y.C., Kirkegaard, K. & Wang, J.C. Covalent bonds between protein and DNA: formation of phosphotyrosine linkage between certain DNA topoisomerases and DNA. *J. Biol. Chem.* **255**, 5560–5565 (1980).
30. Yang, J., Bachrati, C.Z., Ou, J., Hickson, I.D. & Brown, G.W. Human topoisomerase III α is a single-stranded DNA decatenase that is stimulated by BLM and RMI1. *J. Biol. Chem.* **285**, 21426–21436 (2010).
31. Hoadley, K.A. *et al.* Structure and cellular roles of the RMI core complex from the Bloom syndrome dissolvosome. *Structure* **18**, 1149–1158 (2010).
32. Wang, F. *et al.* Crystal structures of RMI1 and RMI2, two OB-fold regulatory subunits of the BLM complex. *Structure* **18**, 1159–1170 (2010).
33. Lima, C.D., Wang, J.C. & Mondragon, A. Three-dimensional structure of the 67K N-terminal fragment of *E. coli* DNA topoisomerase I. *Nature* **367**, 138–146 (1994).
34. Hansen, G., Harrenga, A., Wieland, B., Schomburg, D. & Reinemer, P. Crystal structure of full length topoisomerase I from *Thermotoga maritima*. *J. Mol. Biol.* **358**, 1328–1340 (2006).
35. Mondragón, A. & DiGate, R. The structure of *Escherichia coli* DNA topoisomerase III. *Structure* **7**, 1373–1383 (1999).
36. Aravind, L., Leipe, D.D. & Koonin, E.V. Toprim: a conserved catalytic domain in type IA and II topoisomerases, DnaG-type primases, OLD family nucleases and RecR proteins. *Nucleic Acids Res.* **26**, 4205–4213 (1998).
37. Duguet, M., Serre, M.C. & Bouthier de La Tour, C. A universal type IA topoisomerase fold. *J. Mol. Biol.* **359**, 805–812 (2006).
38. Schultz, S.C., Shields, G.C. & Steitz, T.A. Crystal structure of a CAP-DNA complex: the DNA is bent by 90 degrees. *Science* **253**, 1001–1007 (1991).
39. Brennan, R.G. & Matthews, B.W. The helix-turn-helix DNA binding motif. *J. Biol. Chem.* **264**, 1903–1906 (1989).
40. Flynn, R.L. & Zou, L. Oligonucleotide/oligosaccharide-binding fold proteins: a growing family of genome guardians. *Crit. Rev. Biochem. Mol. Biol.* **45**, 266–275 (2010).
41. Goulaouic, H. *et al.* Purification and characterization of human DNA topoisomerase III α . *Nucleic Acids Res.* **27**, 2443–2450 (1999).
42. Changela, A., DiGate, R.J. & Mondragon, A. Crystal structure of a complex of a type IA DNA topoisomerase with a single-stranded DNA molecule. *Nature* **411**, 1077–1081 (2001).
43. Changela, A., DiGate, R.J. & Mondragon, A. Structural studies of *E. coli* topoisomerase III-DNA complexes reveal a novel type IA topoisomerase-DNA conformational intermediate. *J. Mol. Biol.* **368**, 105–118 (2007).
44. Schmidt, B.H., Burgin, A.B., Deweese, J.E., Osheroff, N. & Berger, J.M. A novel and unified two-metal mechanism for DNA cleavage by type II and IA topoisomerases. *Nature* **465**, 641–644 (2010).
45. Li, Z., Mondragon, A., Hiasa, H., Marians, K.J. & DiGate, R.J. Identification of a unique domain essential for *Escherichia coli* DNA topoisomerase III-catalysed decatenation of replication intermediates. *Mol. Microbiol.* **35**, 888–895 (2000).
46. Feinberg, H., Lima, C.D. & Mondragon, A. Conformational changes in *E. coli* DNA topoisomerase I. *Nat. Struct. Biol.* **6**, 918–922 (1999).
47. Xiong, B. *et al.* The type IA topoisomerase catalytic cycle: A normal mode analysis and molecular dynamics simulation. *Proteins* **71**, 1984–1994 (2008).
48. Li, Z., Mondragon, A. & DiGate, R.J. The mechanism of type IA topoisomerase-mediated DNA topological transformations. *Mol. Cell* **7**, 301–307 (2001).
49. Viard, T. & de la Tour, C.B. Type IA topoisomerases: a simple puzzle? *Biochimie* **89**, 456–467 (2007).
50. Bolanos-Garcia, V.M. *et al.* Spatial and temporal organization of multi-protein assemblies: achieving sensitive control in information-rich cell-regulatory systems. *Philos. Trans. A Math. Phys. Eng. Sci.* **370**, 3023–3039 (2012).

ONLINE METHODS

Protein expression prior to crystallization. Human Strep-TopIII α (residues 1–753)–RMI1 (residues 1–219) complex was coexpressed in High Five insect cells with a pFastBac dual transfer vector (Bac-to-Bac system, Invitrogen). Cells were infected at a concentration of 4×10^6 cells/ml and harvested after 48 h after infection. Lysis in 50 mM Tris-HCl, pH 8.0, 200 mM NaCl, 1 mM β -mercaptoethanol, 1 mM PMSF and protease inhibitor cocktail (Sigma) was performed by sonication, and lysates were subsequently clarified by ultracentrifugation. Streptactin affinity purification was performed as a first strep-affinity step. This was followed by POROSQ anion-exchange chromatography (buffered by 50 mM Tris, pH 8.0, 0.2 mM TCEP) to remove traces of endogenous DNA. As a final step, the purified protein was subjected to size-exclusion chromatography on a Superdex 200 column (GE Healthcare) (50 mM HEPES, pH 7.4, 300 mM NaCl, and 0.2 mM TCEP). Fractions containing the heterodimeric complex were pooled and subjected to crystallization experiments.

Complex crystallization. The complex (8 mg/ml) was crystallized in 8–12% (w/v) PEG 2000, 100 mM Tris-HCl, pH 7.0, and 200 mM MgCl₂. Crystals grew only in the presence of Mg²⁺ or Ca²⁺. The conditions of crystallization for the crystals grown in the presence of Ca²⁺ were Tris, pH 7.0, 8% (w/v) PEG 5000 MME, and 200 mM calcium citrate. Crystals in either Mg²⁺ or Ca²⁺ appeared as square-based rods growing to maximal dimensions within 4–5 d. Cryopreservation of crystals was performed by supplementation of the growth condition with 35% ethylene glycol before flash cooling in liquid nitrogen.

Data collection and processing. X-ray diffraction data were recorded with a Pilatus 6M detector (Dectris) at beamline PXII of the Swiss Light Source (Villigen, Switzerland) with a wavelength of 1.0 Å. Data sets from crystals grown in the presence of Mg²⁺ (TOPIII α –Mg²⁺–RMI1) and Ca²⁺ (TOPIII α –Ca²⁺–RMI1) were collected. Data were processed with XDS⁵¹, and POINTLESS⁵² was used for space-group prediction and format conversion before additional scaling and merging with AIMLESS⁵². Averaged intensities were converted to structure-factor amplitudes by TRUNCATE⁵².

Both data sets are strongly anisotropic. Analyzed in the true space group, *P*₄₁₂₁₂, the resolution at which $\langle I/\sigma \rangle = 2$ for the TopIII α –Mg²⁺–RMI1 data is 3.16 Å along the *ab* plane and 2.63 Å along the *c* axis, the two principal directions for anisotropy in tetragonal crystals. When represented as a thermal ellipsoid, the difference (ΔB) is 26.6 Å². The TOPIII α –Ca²⁺–RMI1 data have a $\Delta B = 24.0$ Å² and resolution limits of 3.64 Å along the *ab* plane and 2.88 Å along the *c* axis. The anisotropy resulted in high merging *R* factors for both data sets. However, over the resolution range defined by the anisotropic $\langle I/\sigma \rangle = 2$ cutoff the CC_{1/2} (correlation coefficient between random half data sets⁵³) remained greater than 0.4. This suggests that there is substantial useful signal at high resolution. Final data-processing statistics are given in Table 1. 96.7% and 96.0% of residues were in the favored regions of the Ramachandran plot for TOPIII α –Mg²⁺–RMI1 and TOPIII α –Ca²⁺–RMI1, respectively, with 0% and 0.1% outliers, respectively.

Structure determination and refinement. The TopIII α –Mg²⁺–RMI1 structure was solved by molecular replacement (MR) in space group *P*₄₁₂₁₂ with PHASER⁵⁴ with an *E. coli* Top1A³³ search model proposed by BALBES and prepared with CHAINSAW and a search model based on hRMI1 (PDB 3NBI).

The initial TopIII α –Mg²⁺–RMI1 model was iteratively rebuilt with COOT⁵⁵ and refined with PHENIX.REFINE⁵⁶ or REFMAC⁵⁷ at 3.3-Å resolution, at which the outermost resolution shell R_{merge} was less than 50%. After efforts to improve the initial 3.3-Å model stalled, the data were reassessed with the ‘paired-refinement’ strategy of Karplus and Diederichs⁵³ with autoBuster, and an optimal high-resolution limit of 2.85 Å was found. At this resolution, the outermost resolution shell (2.97–2.85 Å) in the direction of the *ab* plane CC_{1/2} was 0.30, and along the *c* axis the CC_{1/2} was 0.97, with an overall CC_{1/2} of 0.81 and a ΔB of 25.9 Å². Inclusion of the weak high-resolution data in refinement markedly improved the quality of the refined models and the interpretability of the electron density maps. This revealed $mF_o - DF_c$ difference-map peaks for the water molecules coordinated by the Mg²⁺ ion and for an additional 39 water molecules and enabled the correction of several side chain rotamers. The final TopIII α –Mg²⁺–RMI1 model was produced after iterative model building with COOT and refinement with autoBuster (<http://www.globalphasing.com/buster/>) with data to 2.85-Å resolution,

one TLS group per chain. The TopIII α –Ca²⁺–RMI1 crystal structure was determined by rigid-body fitting of the TopIII α –Mg²⁺–RMI1 data at 3.25-Å resolution, selected with similar CC_{1/2} cutoffs derived for TopIII α –Mg²⁺–RMI1 (in the outer resolution shell (3.45–3.25 Å), a CC_{1/2} of 0.24 in the direction of the *ab* plane and a CC_{1/2} of 0.97 in the direction of the *c* axis, with an overall CC_{1/2} of 0.73 and a ΔB of 35.5 Å²). The TopIII α –Ca²⁺–RMI1 model was rebuilt and refined in the same way as for TopIII α –Mg²⁺–RMI1 with the addition of local structure similarity restraints imposed on the final TopIII α –Mg²⁺–RMI1 model. The metal sites in both structures were restrained to maintain octahedral geometry and appropriate bond lengths (Mg²⁺–OH₂ = 2.09 Å and Ca²⁺–OH₂ = 2.42 Å, both with $\sigma = 0.02$ Å), and the same randomly assigned set of 5% of all reflections was omitted from refinement for cross-validation. MolProbity⁵⁸, used to analyze model quality, places the TopIII α –Ca²⁺–RMI1 model in the 100th percentile, among the best for this resolution.

The RMI1 decatenation loop (residues 116–130) was ordered in the TopIII α –Ca²⁺–RMI1 crystal as opposed to that of TopIII α –Mg²⁺–RMI1, thus allowing the loop to be traced. The final refined model contains RMI1_{2–216} and TopIII α _{20–637} with one hydrated Mg²⁺/Ca²⁺ ion bound to Glu41 in monodentate mode. Several side chains were truncated at C β , owing to a lack of electron density, and additional residues of the TopIII α N and C termini that could not be unequivocally built were omitted from the model. Refinement statistics for the final models are given in Table 1.

Electron microscopy. The sample used for crystal growth was diluted to a concentration of 200 nM in 25 mM HEPES, pH 7.4, 100 mM NaCl and 0.2 mM TCEP immediately before it was applied to glow-discharged holey carbon grids (Cu 400-mesh grids, Quantifoil Micro Tool GmbH). The protein was adsorbed to the EM grids for 45 s and negatively stained with 2% (m/w) uranyl acetate solution. The grid was examined with a Philips CM10 electron microscope equipped with a LaB6 filament and operated at 80 kV. Images were recorded as CCD micrographs at 130,000 \times nominal magnification, resulting in a pixel size of 3.7 Å. A total of 4,000 particles were picked and subsequently analyzed with EMAN2. To avoid model bias, the initial model used for angular refinements was a featureless Gaussian blob with dimensions estimated from the crystal structure of TopIII α –RMI1, generated with the command `makeinitialmodel.py` as implemented in EMAN. After several cycles of refinement convergence, the final model (Supplementary Fig. 3) was obtained. The angular spacing used for orientation generation was set to 10°. Smaller increments did not improve the model further.

Relaxation, M13 digest assays and catenation-decatenation assays with yeast proteins. Yeast Top3, Sgs1 and bacterial SSB were expressed and purified as outlined in ref. 23. Yeast Rmi1 WT and rl constructs were expressed in insect cells (High Five) as GST N-terminal fusion proteins with C-terminal His₆ tags, according to a previously described protocol²³ to avoid nuclease contamination. Proteins were stored in 50 mM Tris, pH 7.0, 150 mM NaCl, 1 mM β -mercaptoethanol, and 10% glycerol (final buffer). For the relaxation assay, proteins (Top3 and different Rmi1 constructs) were incubated in the presence of substrate PUC19 (200 ng per reaction) and incubated 1 h at 42 °C in reaction buffer (25 mM HEPES, pH 7, 100 μ g/ml BSA, 32% glycerol, 5 mM NaOAc, and 0.5 mM MgOAc). The reactions were stopped by the addition of EDTA and Proteinase K and incubation for 1 h at 37 °C. The samples were run on 1% agarose gel in the presence or absence of EtBr.

M13 (200 ng per reaction, M13 mp18 phage ssDNA from Clontech) digestions were performed for 1 h, 3 h or overnight in a reaction buffer of 25 mM HEPES, pH 7.4, 100 μ g/ml BSA, 32% glycerol, 5 mM NaOAc, and 2 mM MgOAc. The reactions were stopped by incubation with EDTA and Proteinase K for 1 h at 37 °C. The gels were stained with SYBR Green II (Life Technologies). For the catenation assays, 100 nM Top3, 60 nM Sgs1 and 1 μ M *E. coli* SSB (Sigma) were incubated alone or with 200 nM GST–WT Rmi1 or GST–rlRmi1 in the presence of 100 ng pUC19, as described previously²⁵. The decatenation assays were performed as the catenation assays were, but in the presence of 100 ng of kDNA (Topogen). Products were loaded on a 1% agarose gel in the presence of EtBr.

Dissolution of double Holliday junctions. The human L₁ and L₂ RMI1-loop variants were generated by a site-directed mutagenesis strategy, cloned in pGEX

plasmids and produced in *E. coli* ROSETTA strain (overnight expression at 20 °C after induction with 0.2 mM IPTG). The cells were harvested and lysed by sonication. After ultracentrifugation clarification, a GST-Sepharose affinity step was performed. This was followed by overnight TEV cleavage (4 °C, 2% of TEV protease). RMI1 protein was further purified by anion-exchange chromatography (POROS Q resin, GE Healthcare) allowing the separation of GST tag (elution around 140 mM NaCl) from RMI1 (elution around 200 mM NaCl). The proteins were dialyzed overnight against final buffer.

The dHJ substrate preparation and dissolution reactions were carried out as described in ref. 59 with the exception that the reaction products were separated with 8% native acrylamide gel electrophoresis run at 4 °C. After being dried, the gels were exposed overnight to a phosphorimager screen, and the image was recorded with a Typhoon scanner. The stimulation factor (represented in Fig. 4g) was calculated as the percentage of product formed in the presence of RMI1 divided by the percentage of product observed in the absence of RMI1.

51. Kabsch, W. Automatic processing of rotation diffraction data from crystals of initially unknown symmetry and cell constants. *J. Appl. Crystallogr.* **26**, 795–800 (1993).
52. Winn, M.D. *et al.* Overview of the CCP4 suite and current developments. *Acta Crystallogr. D Biol. Crystallogr.* **67**, 235–242 (2011).
53. Karplus, P.A. & Diederichs, K. Linking crystallographic model and data quality. *Science* **336**, 1030–1033 (2012).
54. McCoy, A.J. *et al.* Phaser crystallographic software. *J. Appl. Crystallogr.* **40**, 658–674 (2007).
55. Emsley, P., Lohkamp, B., Scott, W.G. & Cowtan, K. Features and development of Coot. *Acta Crystallogr. D Biol. Crystallogr.* **66**, 486–501 (2010).
56. Adams, P.D. *et al.* PHENIX: a comprehensive Python-based system for macromolecular structure solution. *Acta Crystallogr. D Biol. Crystallogr.* **66**, 213–221 (2010).
57. Murshudov, G.N., Vagin, A.A. & Dodson, E.J. Refinement of macromolecular structures by the maximum-likelihood method. *Acta Crystallogr. D Biol. Crystallogr.* **53**, 240–255 (1997).
58. Chen, V.B. *et al.* MolProbity: all-atom structure validation for macromolecular crystallography. *Acta Crystallogr. D Biol. Crystallogr.* **66**, 12–21 (2010).
59. Bachrati, C.Z. & Hickson, I.D. Dissolution of double Holliday junctions by the concerted action of BLM and topoisomerase III α . *Methods Mol. Biol.* **582**, 91–102 (2009).